



Melnyk, O., Jones, R., Macedo, R. , Garbovskiy, Y., Hagen, G., Glushchenko, A. V., Spendier, K. and Camley, R. E. (2021) Fast switching dual-frequency nematic liquid crystal tunable filters. *ACS Photonics*, 8(4), pp. 1222-1231. (doi: [10.1021/acsphotonics.1c00151](https://doi.org/10.1021/acsphotonics.1c00151))

The material cannot be used for any other purpose without further permission of the publisher and is for private use only.

There may be differences between this version and the published version. You are advised to consult the publisher's version if you wish to cite from it.

<http://eprints.gla.ac.uk/238429/>

Deposited on 09 April 2021

Enlighten – Research publications by members of the University of
Glasgow

<http://eprints.gla.ac.uk>

Fast switching dual-frequency nematic liquid crystal tunable filters

Olha Melnyk^{,a}, Reed Jones^a, Rair Macêdo^b, Yuriy Garbovskiy^c, Guy Hagen^a, Anatoliy V. Glushchenko^a,
Kathrin Spendier^a, Robert E. Camley^a*

^aUCCS Biofrontiers Center and Department of Physics and Energy Science, University of Colorado
Colorado Springs, Colorado Springs, 80918, CO, USA;

^bJames Watt School of Engineering, Electronics & Nanoscale Engineering Division, University of
Glasgow, Glasgow, G12 8QQ, United Kingdom;

^cDepartment of Physics and Engineering Physics, Central Connecticut State University, New Britain,
06050, CT, USA

*omelnyk@uccs.edu

ABSTRACT: We develop tunable optical filters with dual-frequency nematic liquid crystal optical retarders to enable fast switching between the passed wavelengths. The filters are composed of a series of two liquid crystal optical retarders. We select the specific thicknesses of the liquid crystal retarders and use individual biasing schemes to continuously tune the wavelength and bandwidth of the filter.

This enables fine-tuned filter switching speeds of filter operation in the ms regime. We present theoretical predictions and experimental results for the electro-optical filter characterization as well as an example application for our filter in total internal reflection fluorescence microscopy. We find that our filter switching speeds can be as short as a few ms, an order of magnitude improvement over typical mechanical filter wheel switching speeds. The quality of our fluorescence images is similar to those obtained by conventional filters.

KEYWORDS: liquid crystals, dual-frequency nematics, tunable filters, TIRF microscopy, cell imaging.

Introduction

Fast switching optical filters are of significant interest for multiple applications in various fields, from biomedical imaging and microscopy (1–3) to light detection and ranging (LIDAR) systems (4,5). Modern applications require multispectral, narrowband, tunable devices with fast switching speeds. Different technologies have been used to produce rapid switching bandpass filters in the visible optical range: starting from interference-based filters to optical mode coupling filters (6–8). For the applications we are considering – multispectral and hyperspectral imaging, biomedical spectroscopy, and microscopy – the most promising types of fast tunable filters in the literature are acousto-optical tunable filters (AOTF) and liquid crystal tunable filters (LCTF). AOTF and LCTF have their advantages and drawbacks depending on the application (9–11). Even though AOTF has faster transition times compared to LCTF, their typical aperture size and image quality are lower than for the LC-based filters and therefore are not appropriate for biological microscopy (10). In addition, AOTF is typically more complicated in operation and expensive in production compared to LCTF. A detailed comparison of AOTF and LCTF is given in Ref. 10.

Several types of LC-based optical filters have been presented in recent years. Two major approaches for LCTF designs can be distinguished:

- Modification of the filter architecture (transmission structure, reflection structure, cavity structure, etc.) (12–20)
- Modification of the LC material (i.e. choice of nematics, smectics, functional LC-based materials, metamaterials) (21–24)

In this paper, we discuss the design, characteristics, and applications for a novel LC tunable filter which is based on dual-frequency nematic liquid crystals (DFNLC). The advantage of DFNLC is that they have significantly faster switching times (25) because the switching can be accomplished by varying both the biasing voltage amplitude and the biasing frequency, typically in the 0.1 – 100 kHz range. The filter has a novel biasing scheme which utilizes the fact that the effective orientation of the DFNLC depends on the

frequency of the biasing voltage (26). The replacement of ordinary nematic LC with DFNLC has proven to have advantages in multiple LC devices (27,28).

Our electrically tunable filter has a millisecond time response — about an order of magnitude faster than current mechanical switching filters and typical LCTF, and comparable to the operation times of the AOTF. Here, we will show how these filters could be applied in the fluorescence microscopy field with a substantially improved time resolution. Fluorescence microscopy is used to image live cells with high resolution and requires fast tunable optical components (29–31). Live cells can be imaged on a few ms timescales by image splitters or beam splitters (32,33), however, both systems have drawbacks. Image splitters reduce the field of view because two or four separate, spatially identical images are displayed as two or four quadrants on a single camera chip. Beam splitter set-ups require multiple cameras, one for each fluorescent emission spectra. A multiple camera set-up is significantly more expensive than a single camera set-up and therefore electrically tunable filters are a better choice for given experiments.

Historically the application of the LC to the tunable filters started with Lyot (34) and Solc (35) structured passive filters. The main idea in these early works was to combine LC layers between crossed polarizers and determine the total transmittance of the configuration, taking into account the LC material and layer parameters (13). We are concentrated on the active filter scheme, so the thickness selection of the LC layer plays a smaller role in our design. In addition, earlier filters typically used standard nematic liquid crystals. Our use of DFNLC provides two new aspects for the filter:

- the time response is faster;
- the LC birefringence can be adjusted by both the magnitude and frequency (typically in the low kHz range) of the biasing voltage.

To produce an optical filter, DFNLC optical retarders were used as shown in Fig. 1. The polarization interference principle is used for wavelength selected transmittance of the filter. The LC retarder consists of two crossed polarizers with a LC layer sandwiched in between. Unpolarized light, passing through a first polarizer in a retarder, becomes linearly polarized, and then experiences change in its state of polarization due to the birefringence of the LC layer. This state of polarization depends on multiple

factors: the wavelength of incoming light, the LC layer thickness, and the orientation of the LC molecules. The amount of light passing through the retarder depends on the direction of the second polarizer and the polarization state of the electromagnetic wave after it passes through the liquid crystal. Because the final polarization state depends on the frequency of the incoming light, this can lead to a wavelength selection process where only certain frequencies/wavelengths are passed through the filter.

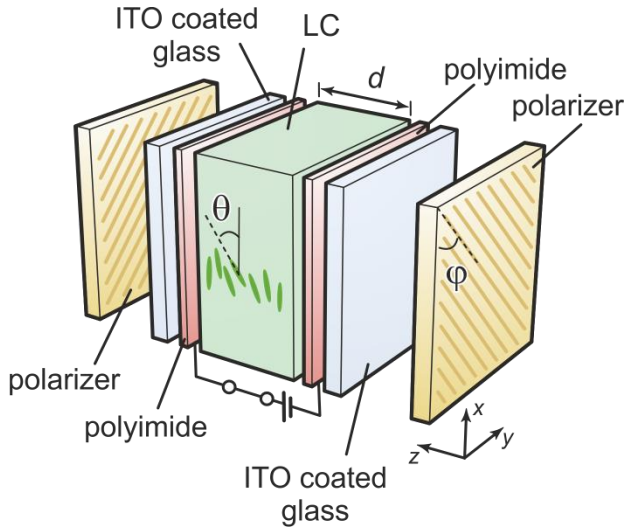


Figure 1. Schematic structure of the LC retarder where a LC cell is placed between two crossed polarizers. The LC cell comprises a LC sandwiched between two glass substrates, each covered with an indium tin oxide (ITO) layer and a polyimide layer.

Here, we used two optical retarders to produce a usable filter that had a single bandpass region in the wavelength of interest (a full description of the device preparation is given in the Methods section). By selecting different DFNLC cell thicknesses, a wider or narrower bandpass selection can be achieved. It is important to note that the addition of more retarders will decrease the transmission of the filter due to the increased number of polarizers. For most optical applications, the transmittance level is as important as the speed of filter transition. Therefore, we decided to stay with a system limited to two retarders. In addition, thicker LC layers increase the bandpass selection region with narrower passing/blocking windows, but with a decrease in filter operation speed as well as transmittance. Because of this, we decided to fine-tune the filter through an active driving scheme. Using DFNLCs, we can control the

orientation of LC molecules with higher efficiency and achieve ms transition times. Theoretical calculations of the various LC retarders and filters behavior under applied external electric field were performed as well (these are described in detail in the Methods section).

Results.

We start by looking at the electro-optical response of the LC retarder to a single incident wavelength. This allows us to correlate our theoretical predictions to the experimental results. The set-up used here is a conventional electro-optical response measurement system consisting of a He-Ne laser (wavelength 632 nm), a retarder, and a photodetector in a straight optical path configuration (36) as shown in Fig. 2(a). For biasing of the LC retarder, a proprietary driving system was used.

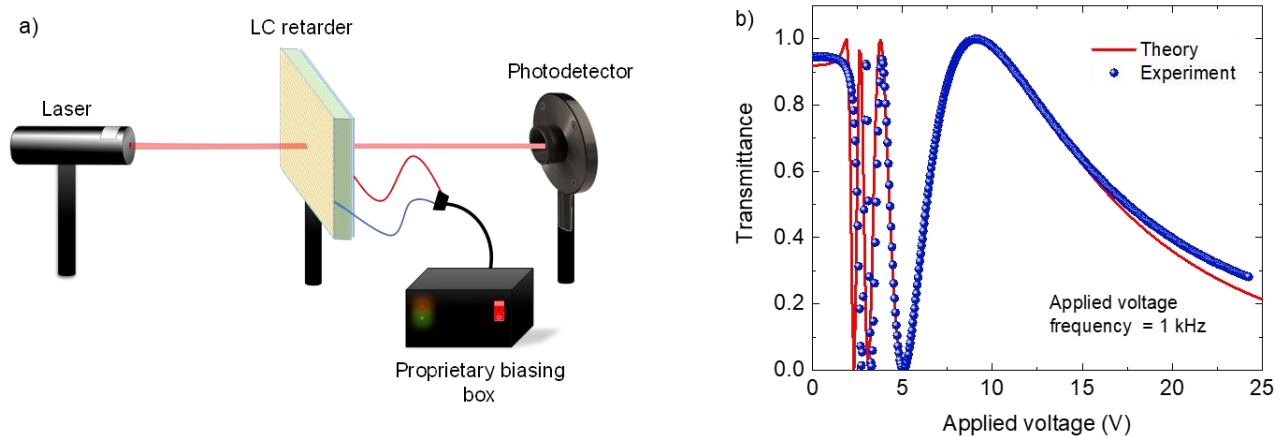


Figure 2. (a) Schematics of the electro-optical measurement system composed of a He-Ne laser (wavelength 632 nm), a retarder, and a photodetector in a straight optical path configuration. The proprietary biasing box is used to apply voltage V to the retarder. (b) Transmittance as a function of the applied voltage for a $10.4 \mu\text{m}$ LC retarder. The frequency of the applied voltage waveform is 1 kHz (square waveform). The solid red line is our theoretical calculation (see details and parameters in the Methods section), and the blue solid spheres are experimental data.

Results of the measured (blue spheres) and calculated (red line) transmittance as a function of the applied voltage to the LC retarder are presented in Fig. 2(b). Here and throughout the paper we use the DFNLC material MLC-2048 from Merck. This figure illustrates the typical response of the LC retarder to an applied voltage. Because most of the rotation of LC molecules happens at low voltages (below 5 V), we observe fast changes in the transmittance intensity in the form of multiple oscillations. In fact, one peak corresponds to a 2π change in retardation. By changing the applied voltage, the retardation can be controlled in a desirable way (37). Note that no significant changes are seen between 0 and 2 V as this is

the threshold voltage for this configuration (38). At high voltages, the molecules have almost fully rotated, which leads to a vanishing transmission. As it can be seen, our theoretical calculations are in excellent agreement with measured results. Therefore, from this point forward we use them to accurately predict the behavior of our LC devices.

We then move to a second experiment where we measure the transmittance spectra of our LC retarders using a UV-visible-IR spectrophotometer with a 1 nm spectral resolution (Lambda 1050 from PerkinElmer). The LC retarders were placed in the spectrophotometer and continuous transmittance was measured for the spectral range from 450 nm to 650 nm, which is the spectral range of operation of the polarizers used to produce this device.

First, we measure the transmittance of the individual retarders with different biasing voltages and frequencies of a square waveform. This is shown in Fig. 3, where the experimental data (spheres) is compared to theoretical results (lines). Fig. 3(a) shows a comparison of the transmittance spectra for a fixed applied voltage amplitude of 2.8 V at three different biasing frequencies. At a frequency of 1 kHz, we can see that the peak of transmittance is just above 500 nm (shown in blue). As we increase the frequency, inducing a decrease in dielectric anisotropy of DFNLC, the transmittance peak is shifted to higher wavelengths – at 550 nm for 5 kHz (shown in green) and 600 nm for 9 kHz (shown in magenta). Note that for higher frequencies of the voltages, exemplified by the magenta curves, two peaks are now observed. Here we are interested in the first-order interference peak, which is the one with a wider half-maximum width. In Fig. 3(b) we show the behavior of the LC retarder transmittance for a fixed frequency (1 kHz) and different amplitudes of applied voltages. We can see that the peak in the transmittance spectrum is now shifted to lower wavelengths as the voltage is increased, starting at 600 nm for 2.1 V (shown in blue) and decreasing to 540 nm for 2.6 V (shown in magenta). Again, we are interested in the wider (main) peak of transmittance.

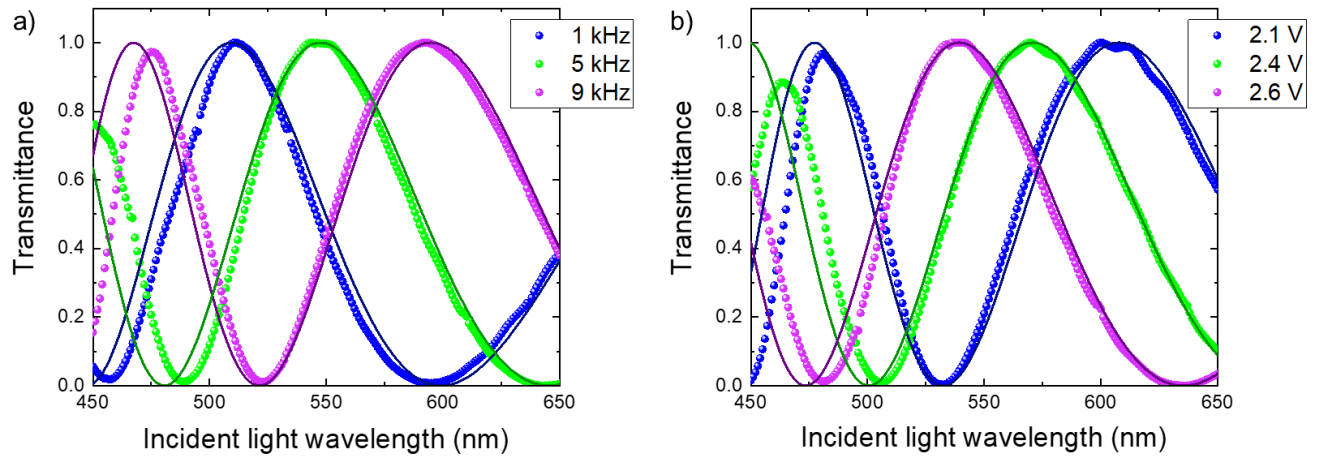


Figure 3. The transmittance of a 7.4 μm retarder as a function of the incident light wavelength with (a) applied voltage of 2.8 V at different biasing frequencies of square waveforms and (b) different biasing voltages at 1 kHz frequency. The spheres are for the experimental data and the lines are for the theory.

We can see that by controlling the amplitude or frequency of the applied biasing voltage, the transmittance curve can be smoothly shifted up or down in wavelength. This allows us to design a filter with a desired transmittance profile and modify it dynamically by changing the biasing voltage or frequency.

Now that we have checked the behavior of a single LC retarder, we move on to designing a DFNLC filter. In the application, discussed below, we are interested in switching between measuring a green fluorescence signal and a red fluorescence signal. As a result, we are interested in a filter with an approximately 20 nm wide transmittance spectra, and a tunable maximum transmittance near two wavelengths: 500 nm and 580 nm. Theoretical predictions show that the bandpass filtering condition can be met with a combination of two 10 μm thick LC retarders and their respective transmittance patterns.

The idea behind our two-retarder filter geometry is to combine the independent transmittance patterns of each retarder to obtain a single transmittance maximum. These transmittance patterns can be seen by the theoretical results shown in Fig. 4(a) where the blue dashed line is for the first retarder (at 2.7 V) and the black dotted line is for the second retarder (at 4.1 V). We used a value of the relative dielectric anisotropy $\Delta\epsilon = 2.06$ to produce such curves, appropriate for a biasing voltage frequency of 3 kHz for

the experimental results. Combining both lines, we obtain the solid green line showing the resultant transmittance peak at the desired wavelength.

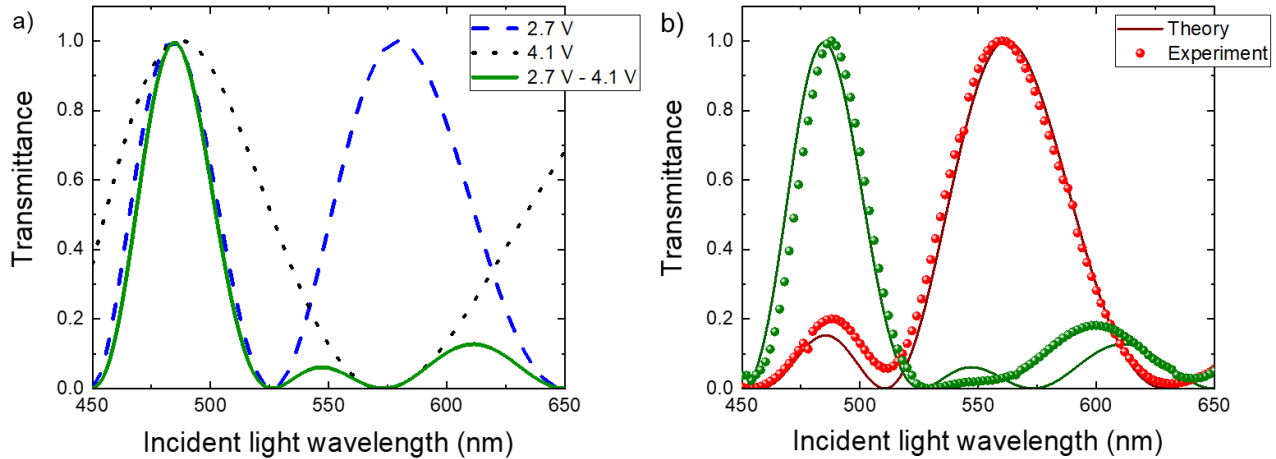


Figure 4. (a) Calculated transmittance as a function of wavelengths for individual retarders and combined filter at different biasing voltages. The blue dashed line produced by applying 2.7 V to the 10.4 μm retarder, the black dotted line – with 4.1 V applied, the solid green line is a resulted spectrum of the combined filter from those retarders. (b) Transmittance as a function of wavelength for a filter combining two 10 μm thick LC retarders with different biasing. The green curves were produced with a voltage amplitude of 2.7 V applied to the first retarder and 4.1 V – applied to the second. The red curves were produced using a voltage amplitude of 2.8 V and 5.1 V applied to the first and second retarder, respectively. The frequency of all applied voltages was 3 kHz. The spheres depict the experimental data and the theory is given by solid lines.

Applying those predictions, we obtained the transmittance spectrum, shown as spheres in Fig. 4(b), displaying two transmittance states. Each state was measured independently by applying a set of voltages with a fixed biasing frequency of 3 kHz. The green curves show maximum transmission just below 500 nm and were obtained using a voltage amplitude of 2.7 V applied to the first retarder and 4.1 V applied to the second retarder. The position of the transmittance peak can be readily modified by changing the voltages at each retarder. As it can be seen from the red curves the peak is moved to 560 nm as we increase the applied voltage to 2.8 V and 5.1 V applied to the first and second retarder, respectively. It is

noteworthy that the shifting of the peaks is seemingly different from that shown in Fig. 3, which is increasing the voltage shifts the transmittance maximum to a higher wavelength. This is because the transmittance maxima, which are seen in Fig. 4(b), are a combination of different order modes of interference as described in the process to obtain the solid green line prediction in Fig. 4(a).

We have shown that a two-retarder system can produce a reasonable transmittance spectrum and act as a filter. This is a quasi-static process, meaning that the voltage is applied for a relatively long time. In this case, the retarder reaches a stable ordered state for each applied voltage and remains that way for the duration of the measurement. In order to achieve fast transition speed for our filters' operation, we now turn to dynamic measurements. For this, we need to investigate the speed at which the filter can transition from one transmittance state to another. However, for the fast switching process, the low voltage driving scheme used earlier is not appropriate (39), and a novel biasing approach is needed.

The transition speed could not be measured with the same equipment used earlier because of limitations in the time acquisition of the spectrophotometer and spectrometer. Therefore, we built a new set-up to measure the transition times. It combines a light source, monochromator, spectrometer, and photodetector. The system configuration is illustrated in Fig. 5. First, a signal from a broadband light source is sent to the monochromator and a specific wavelength is selected. The wavelength resolution of the monochromator is around 25 nm. The light signal then split into two paths using a 50/50 cube. The first one goes to the spectrometer for spectrum measurement and calibration (see an example of the selected wavelengths in Fig. 5) and the second beam passes through the filter and goes to the photodetector to measure the time required for switching the filter. This process is carried out for a range of wavelengths from 450 nm to 650 nm.

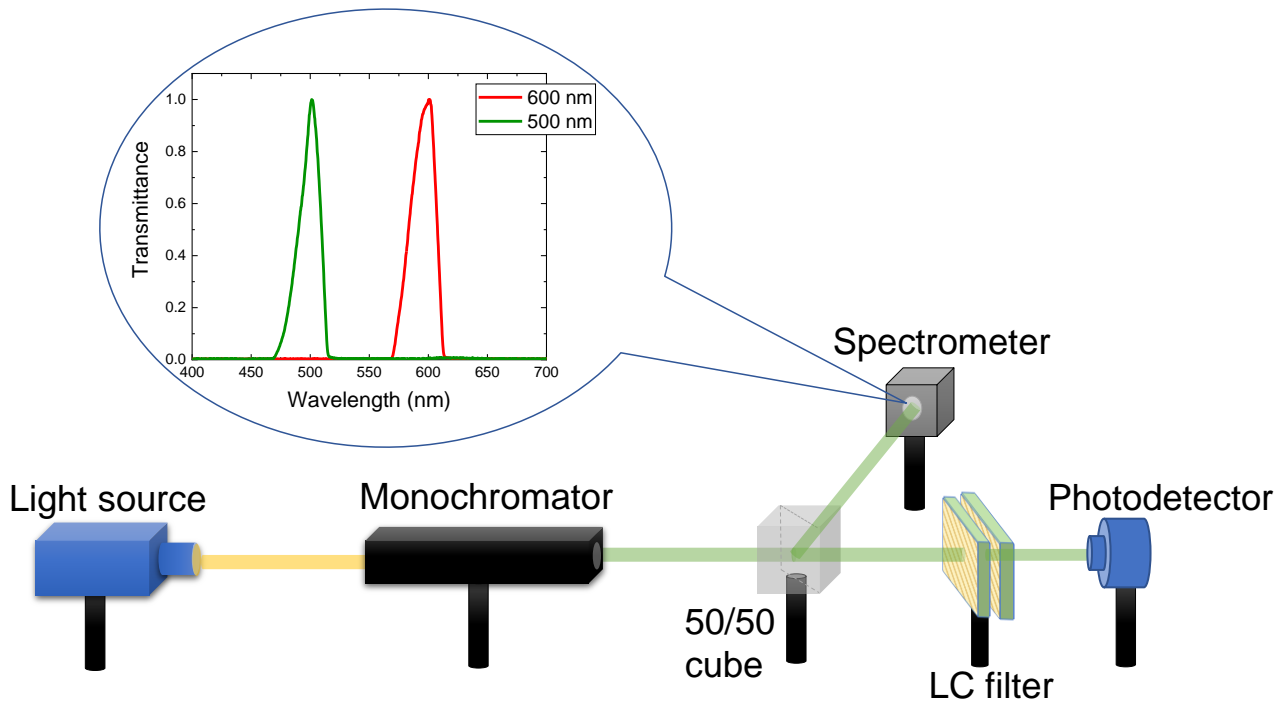


Figure 5. Schematic of the experimental set-up for the dynamic measurements of the filter operation. The inset shows monochromator output for wavelengths of interest as measured by the spectrometer.

Using a custom-designed biasing box, two independent channels with individual biasing voltage waveforms were used to drive the filter, with each retarder having different frequencies, amplitudes, and durations for its voltage profile. The electronics used in the biasing box produced change from one waveform to another with a timeresolution of 0.25 ms. We use an overdriving scheme (40) to facilitate a quick transition from one desired filter wavelength to another. An example of the filter time response at wavelengths of interest is presented in Fig. 6. with details of the applied voltages and waveforms for each retarder given in Table 1.

From Fig. 6, we can see how the transmittance pattern evolves as a function of time. We start displaying a region wherein only green light is allowed through the filter (below 100 ms). This corresponds to Step 3 in Table 1. Then, after changing the voltages through the overdrive scheme: changing through steps 1, 2, and back to 3 again, we obtain maximum transmittance of red light only. The overdrive transition steps are shown as the vertical lines around 100 ms mark and the transition happens within a total time of 8 ms. In order to show the cyclic nature of this process, we show how this repeats again around 200 ms.

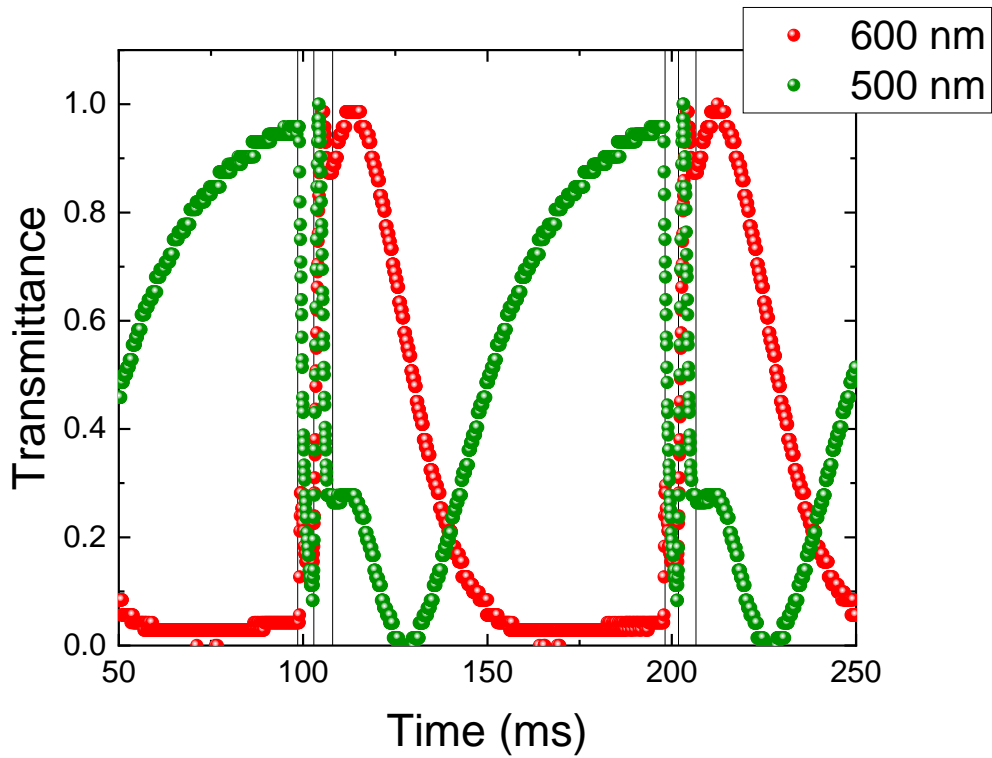


Figure 6. Transmittance as a function of time for the wavelengths of interest. The biasing voltage scheme is given in Table 1. The green spheres represent transmittance of the incoming light with a peak wavelength at 500 nm and the red spheres are for incoming light with a peak wavelength at 600 nm. The vertical black lines indicate the change in the waveform as shown in Table 1 going sequentially through steps 1 to 3.

Table 1. Biasing voltage scheme of the DFNLC filter.

Step	Channel 1 (retarder 1)			Channel 2 (retarder 2)		
	Frequency (kHz)	Amplitude (V)	Duration (ms)	Frequency (kHz)	Amplitude (V)	Duration (ms)
1	1	50	4	1	50	4
2	25	20	4	25	12	4
3	5	20	100	1	5	100

Note that this is one example of a possible voltage scheme. Other schemes can be designed in order to obtain different transmittance patterns with even faster transition times. This is possible due to a large

number of variables in the waveform design that can modify the overall behavior of the filter. The scheme detailed above was designed with a particular application in mind which is now discussed.

Application to Total Internal Reflection Fluorescence (TIRF) Microscopy.

In order to test the applicability of our filters, we have tested them within a TIRF microscope to measure the fluorescence signal of different parts of live biological cells. For this, we used a DMI8 microscope with an oil immersion HCX PL APO 100x/1.47 NA TIRF objective (Leica, Mannheim, Germany)(41). A 1.5x lens was added to the emission beam path resulting in a final magnification of 150x, also we replaced the typical mechanical optical filter wheel with our DFNLC filter. The TIRF module was custom designed by Spectral Applied Research (Ontario, Canada). In the region of the laser light emission, our filter was found to have a relatively high optical density. Therefore, we have combined it with a multiband Chroma 59004m optical filter, which acts as a notch filter for the blue (488 nm) and green (561 nm) laser light. This way, we are able to select one fluorophore signal at a time and observe differently labeled parts of the cell. For image comparison, the same cells were imaged with the commercially available bandpass Chroma filters of similar wavelength operation to our DFNLC filters.

An example of the TIRF microscopy images is presented in Fig. 7 and 8. The test samples are chemically fixed bovine pulmonary artery endothelial (BPAE) cells commercially available from FluoCells. Alexa Fluor 488 phalloidin dye (green) excited by a blue laser was used to stain F-actin, and MitoTracker Red CMXRos dye (red) excited by a green laser was used to stain the mitochondria in the cells. The sCMOS camera (Zyla 4.2+ with IQ software by Andor, Belfast, Northern Ireland) integration time was set to 30 ms.

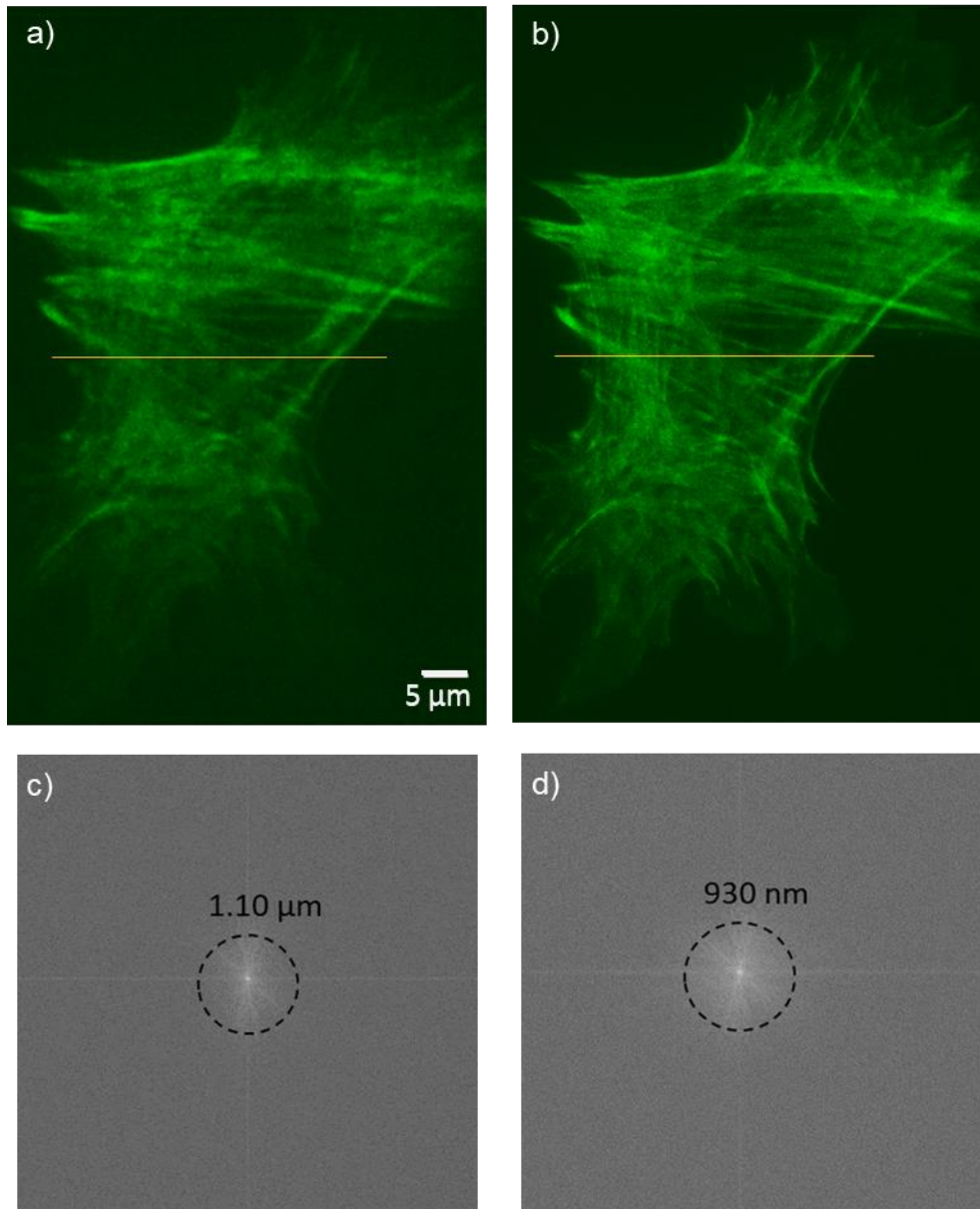


Figure 7. TIRF microscopy images in the highly inclined illumination mode of BPAE cells at a 488 nm laser excitation with (a) our DFNLC filter and (b) with a Chroma ET600 filter, yellow lines indicate the region where the fluorophore signal level was plotted as a function of distance. (c) FFT of the data presented in panel (a); (d) FFT of the data in panel (b). The dashed circles represent the effective resolution of the images.

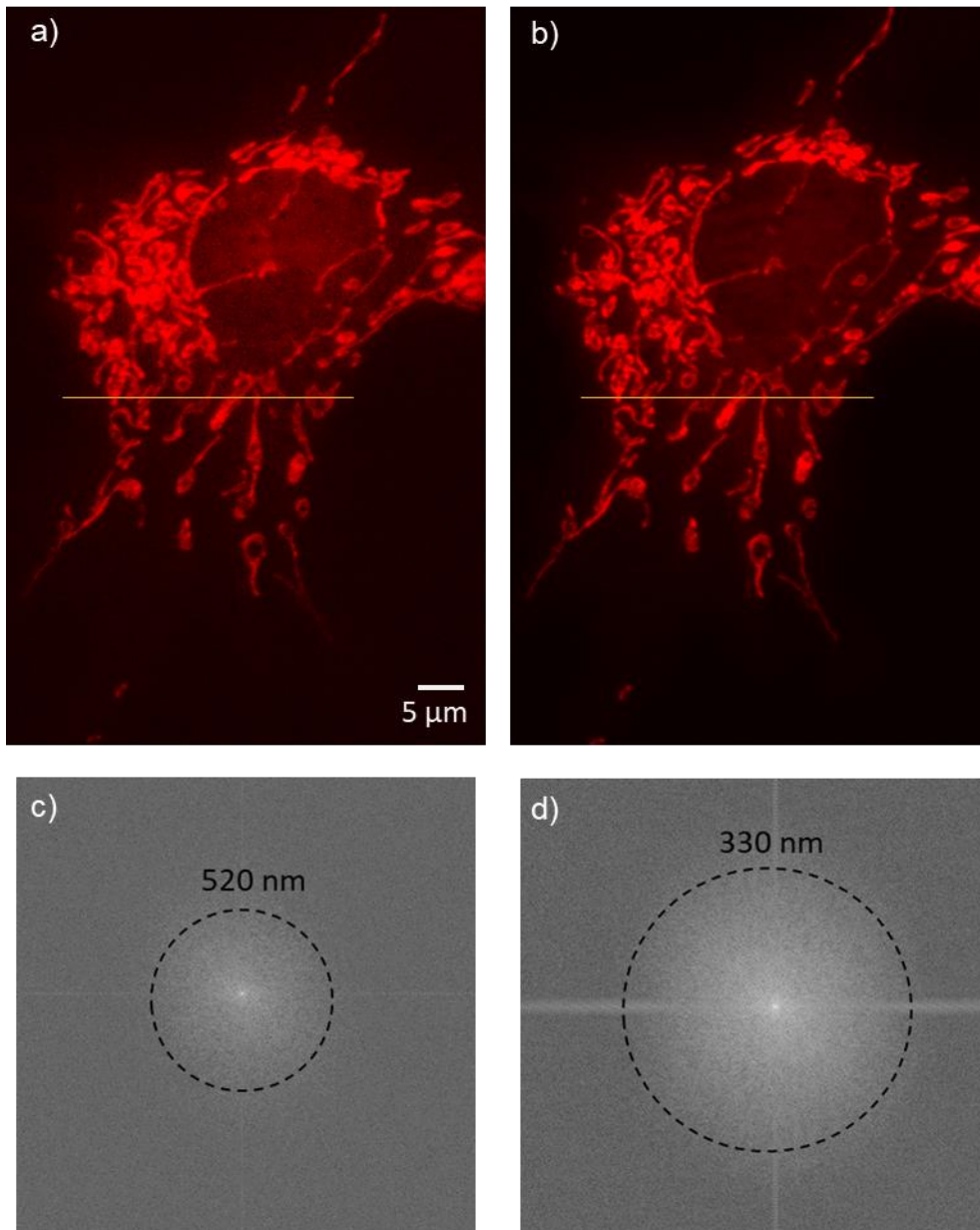


Figure 8. TIRF microscopy images in the highly inclined illumination mode of BPAE cells at a 561 nm laser excitation with (a) our DFNLC filter and (b) with a Chroma ET600 filter, yellow lines indicate the region where the fluorophore signal level was plotted as a function of distance. (c) FFT of the data presented in panel (a); (d) FFT of the data in panel (b). The dashed circles represent the effective resolution of the images.

By image comparison, we can see that the designed DFNLC filter can be successfully applied to TIRF microscopy. The Fourier data for the images were acquired using the fast Fourier transform (FFT) function of the ImageJ software. The effective resolution was determined for each image from this data(42). We

can confirm that the effective resolution of the images obtained with DFNLC filter and Chroma optical filters specified for the fluorescence microscopy are comparable. The signal-to-noise ratio (SNR) of the presented images was calculated as well using the equation:

$$SNR = \frac{\langle I_{signal} \rangle}{\sigma_{background}},$$

where $\langle I_{signal} \rangle$ represents the average signal value from the microscope image and

$\sigma_{background}$ – the standard deviation of the background signal.

Results of the SNR values are presented in Table 2. The SNR calculated for the images obtained with our filter and Chroma filter shows that the image quality is not reduced significantly with the application of the fast tunable filter, but allows a significant improvement of the temporal resolution of the microscopy process.

Table 2. SNR values of the microscope images.

	DFNLC filter	Chroma filters
Alexa Fluor 488 dye	40.12	37.24
MitoTracker Red dye	40.94	46.78

Figure 9 presents a measured fluorophore signal level comparison for the designed DFNLC filter and Chroma filters of the appropriate wavelengths. The measured signal was smoothed and normalized to the maximum signal level on each image for the signal profile comparison. By looking at Fig. 9(a) we can see the signal profile for the parts of the cell labeled with Alexa Fluor 488 phalloidin dye. The main peaks and valleys of the signal measured with different filters are in great agreement and looking at Fig 7 (a) and (b) we are confirming the identity of the microscopy images. The same behavior is confirmed for the MitoTracker Red CMXRos labeled parts of the cell measured with the DFNLC and Chroma filter as well (Fig. 9(b)). With less than 10 ms filter transition times temporal resolution of the dynamical cell imaging can be improved (41).

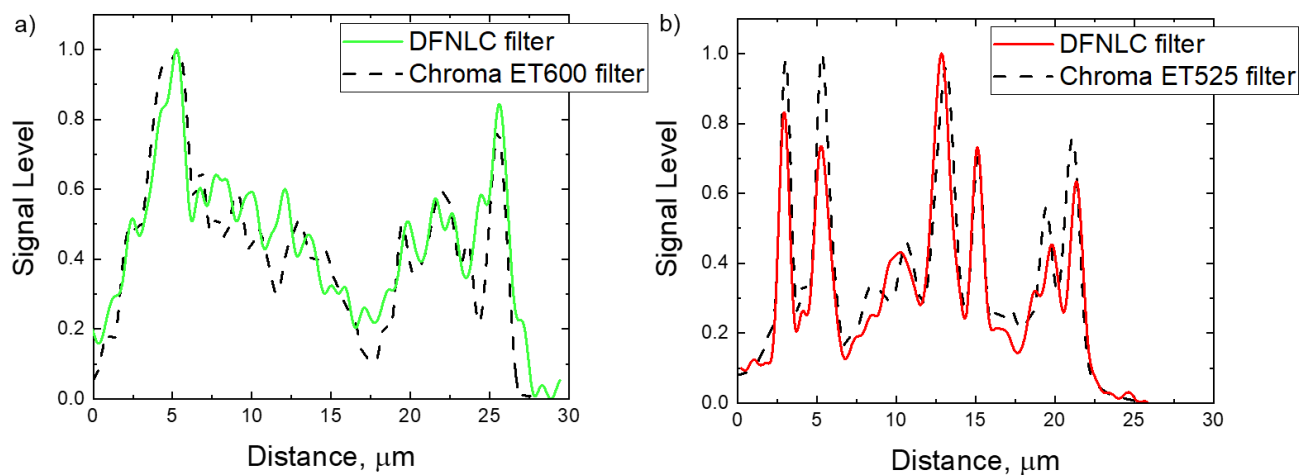


Figure 9. Measured fluorophore signal levels as a function of position: (a) for the Alexa Fluor 488 phalloidin dye measured with designed DFNLC filter (showed in green solid line) and Chroma ET600 filter (showed in dashed black line); (b) for the MitoTracker Red CMXRos dye measured with DFNLC filter (solid red line) and Chroma ET525 filter (dashed black line).

Conclusion and Discussions

In this work, we have provided an efficient method through which it is possible to design tunable, fast switching optical filters based on DFNLC. We have presented an experimental design of a fast bandpass filter for operation in the visible range, with theoretical calculations as a guide. Using the DFNLCs as a birefringent media, we obtain improved control of the electro-optical properties of LC media and achieve specific transmittance spectra by the means of the biasing voltage profiles. The transmittance pattern and timescales of our filter can be readily tuned with a combination of various parameters in the filter driving voltage profile. We expect these properties to also be easily modified through changes in the material properties of the composing DFNLC. We should note that the DFNLC material used to produce the filter prototype was commercially obtained and no changes in its composition were made. However, with material property enhancements, even faster switching speeds can be achieved. We have presented an example application of our filter to illustrate its performance when compared to commercially available filters designed for the application to the TIRF microscopy. For this, we have chosen to image biological live systems (BPAE cells) utilizing TIRF microscopy. However, we expect that these filters can find applicability not only in other fields within biomedical imaging and microscopy but also in other fields such as light detection technology.

We have shown examples of how our filters can be used to image the internal structures of fixed cells; this is a static measurement. We also expect that the filters designed here can be employed in dynamical measurements which could, for example, image the cell membrane behavior during cell-to-cell interaction. Finally, the temporal resolution of our filter (ms), combined with the spatial resolution of TIRF microscopy (nm), offers a new avenue to investigate several biological processes that fall well within this critical time/spatial regime; including protein folding, molecular diffusion, and enzymatic reactions (31).

Methods

LC device preparation.

We prepared single LC cells using the standard planar antiparallel sandwich-like cell configuration. In this, the LC is sandwiched between two glass substrates, each covered with an ITO layer and a polyimide layer. The ITO layers provide conductivity and the rubbed polyimide layers provide an initial orientation and pinning of the LC molecules. The polyimide used was from Nissan Chemicals (ER-1744) for low pre-tilt angles (1 to 3 degrees) and high pinning. This yields a planar initial LC director orientation i.e., the director is oriented parallel to the cell surface. The LC layer thickness was controlled by the glass tube spacers of different diameters. Before filling in a cell, the thickness was confirmed using the interference method of cell thickness measurement (43). MLC-2048 from Merck Ltd was used throughout experiments.

These LC cells were then used to make optical retarders by placing them between crossed polarizers. We chose a geometry wherein the incident light is polarized at a 45° angle with respect to the LC director (shown in Fig. 1). This angle ensures maximum light modulation intensity.

Theoretical models for LC Filters.

The experiments performed throughout this work were conducted at room temperature. Therefore, we have neglected the temperature effects in our theory. We have also used SI units throughout.

For a nematic LC in a cell, the total free energy can be calculated as the sum of the bulk and surface energies, where we assume Rapini Papoular anchoring energy (44,45), given by

$$F = \int_0^d dz U(\theta, \theta') + \frac{1}{2}W \sin^2(\theta - \theta_1) + \frac{1}{2}W \sin^2(\theta - \theta_2), \quad (1)$$

where θ_1 and θ_2 are the pre-tilt angles at the $z = 0$ and $z = d$ surfaces, respectively. Here, the bulk energy density, $U(\theta, \theta')$, is a sum of the Oseen-Frank (elastic) (46,47) and the electric (48) energy densities, and it can be written as:

$$U(\theta, \theta') = \frac{1}{2}(K_{11}\cos^2\theta + K_{33}\sin^2\theta) \left(\frac{d\theta}{dz}\right)^2 - \frac{1}{2}\epsilon_0 E^2(\epsilon_{\perp} - \Delta\epsilon \sin^2\theta). \quad (2)$$

In these equations, $\theta(z)$ is the angle of the director with respect to the substrate (as shown in Fig. 1), $\theta' = d\theta/dz$, W is the anchoring energy, K_{11} and K_{33} are the splay and bend elastic constants, respectively, E is the electric field from the applied voltage, and ϵ_0 is the permittivity of free space. Lastly, $\Delta\epsilon$ is the dielectric anisotropy which is given by $\epsilon_{\parallel} - \epsilon_{\perp}$, where ϵ_{\parallel} is the permittivity measured along the direction parallel to the LC director and ϵ_{\perp} is the permittivity perpendicular to the director, respectively substrate. We note that for DFNLC all the dielectric parameters depend on the frequency of the biasing field. This will be discussed in detail later.

We have solved Eq. (1) for the director profile, $\theta(z)$, by numerically minimizing the free energy F . We used this method because it is much easier to include the anchoring energy, which the experiment tells us is present in our cells. To calculate the derivative θ' , we used a combination of forward and backward difference derivatives. Note that we have neglected any electrostatic charging in the polyimide layers as is often the case in the literature. We also assumed symmetric anchoring energies, leading to symmetric pre-tilt angles.

Alternatively, one can use the Euler-Lagrange equation:

$$\frac{d}{dz} \left(\frac{\partial U}{\partial \theta'} \right) - \frac{\partial U}{\partial \theta} = 0, \quad (3)$$

to derive a steady-state differential equation (39,45) governing $\theta(z)$ along with the boundary conditions.

One finds:

$$\frac{d^2\theta}{dz^2} (K_{11}\cos^2\theta + K_{33}\sin^2\theta) + \left(\frac{d\theta}{dz} \right)^2 (K_{33} - K_{11}) \sin\theta \cos\theta + \epsilon_0 \Delta\epsilon E^2 \sin\theta \cos\theta = 0 \quad (4)$$

In these, the boundary conditions are

$$\left(-\frac{\partial U}{\partial \theta'} + \frac{\partial}{\partial \theta} \left[\frac{1}{2} W \sin^2(\theta - \theta_1) \right] \right) \Big|_{z=0} = 0, \quad (5)$$

and

$$\left(\frac{\partial U}{\partial \theta'} + \frac{\partial}{\partial \theta} \left[\frac{1}{2} W \sin^2(\theta - \theta_1) \right] \right) \Big|_{z=d} = 0. \quad (6)$$

We have checked these two methods against each other and found that both give identical results.

The director profile allows one to calculate an effective index of refraction, n_{eff} , given by(49),

$$n_{eff} = \frac{n_e n_o}{\sqrt{n_e^2 \sin^2 \theta(z) + n_o^2 \cos^2 \theta(z)}} \quad (7)$$

Here the ordinary (o , perpendicular) and extraordinary (e , parallel) indices of refraction are dependent on wavelength (49). A typical plot of the effective index of refraction against biasing voltage is given in Fig. 10. The effective refractive index changes rapidly after the threshold voltage of about 2 V, as seen in Fig. 10 (a). This rapid change accounts for the small difference between the experimental and theoretical results at low voltages. A similar decrease in effective refractive index occurs as the incident light wavelength increases, as seen in Fig 10 (b).

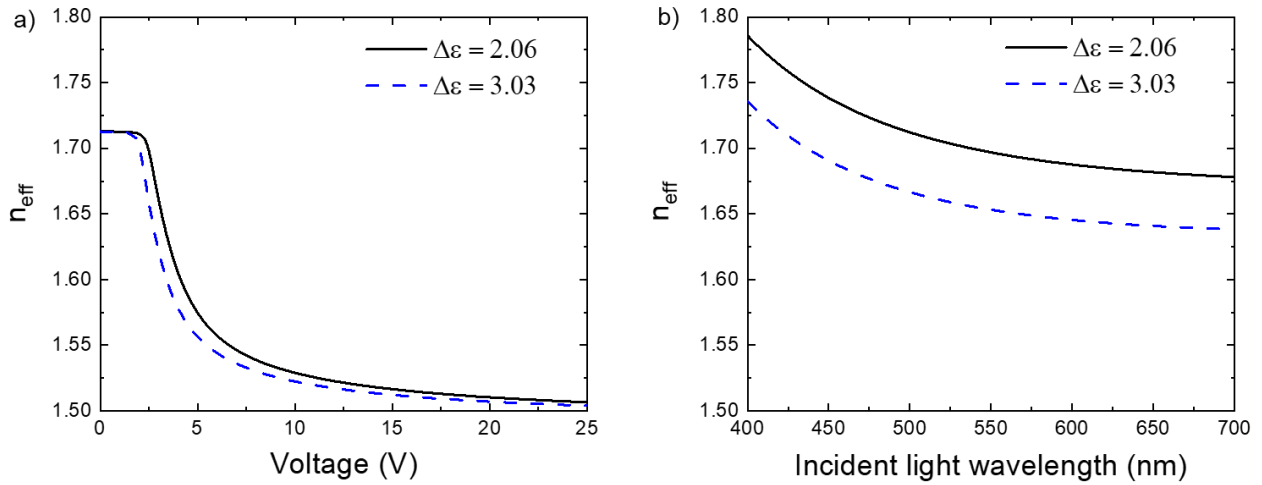


Figure 10. Calculated effective index of refraction (a) as a function of biasing voltage with an incident light wavelength of 632 nm; (b) as a function of incident light wavelength at a biasing voltage of 2.7 V, for a 10.4 μm thick LC cell.

The wavelength-dependent refractive indices are calculated using the extended Cauchy equations(50):

$$n_{e,o} = A_{e,o} + \frac{B_{e,o}}{\lambda^2} + \frac{C_{e,o}}{\lambda^4} \quad (8)$$

Where $A_{e,o}$, $B_{e,o}$, and $C_{e,o}$ are the experimentally determined Cauchy coefficients and λ is the wavelength.

It is then necessary to integrate the effective index of refraction with respect to z over the thickness of the LC layer to determine the transmittance. We split the profile into 101 equally spaced sites and because the number of divisions is even, we can calculate the effective index of refraction integral numerically using Simpson's 1/3 Rule (error of dz^5 (51)). The number of divisions is divisible by four, so we check our accuracy with the higher-order Boole's Rule (52) (error of dz^7 (51)), which confirms the accuracy of Simpson's 1/3 Rule.

For a single LC retarder, as is the case of Fig. 1 and the results discussed in this paper, the transmittance can be found by (49),

$$T = \sin^2 \left[\frac{\pi}{\lambda} \left(\int_0^d dz n_{eff} - n_o d \right) \right] \quad (9)$$

For the filter produced by combining multiple LC retarders, we need a different method to calculate transmittance. The filter has an initial polarizer, a LC film, an intermediate polarizer, a 2nd LC film, and a final polarizer. The experiment is at normal incidence, so we can start by using the Jones Matrix Method (49) to find the intensity transmitted through a single LC cell of thickness d . The incident light is unpolarized and is equal in intensity in both the ordinary and extraordinary directions. Thus, we can write the Jones vector (49),

$$V_{In} = \begin{pmatrix} 1 \\ \frac{1}{\sqrt{2}} \\ 1 \\ \frac{1}{\sqrt{2}} \end{pmatrix}. \quad (10)$$

All polarizers in the filter are linear polarizers. However, as shown in Fig. 2, in our experiment these are taken to be at an angle φ with respect to the x-axis and in the x-y plane. To model this, we can take the typical Jones matrix for linearly polarized radiation along y, given by

$$J_P = \begin{pmatrix} 0 & 0 \\ 0 & 1 \end{pmatrix}, \quad (11)$$

and apply the rotation matrix

$$R(\varphi) = \begin{pmatrix} \cos \varphi & -\sin \varphi \\ \sin \varphi & \cos \varphi \end{pmatrix} \quad (12)$$

to find the rotated polarizer in the x-y plane to be $R(\varphi) J_P R(-\varphi)$.

In the LC layer, the Jones matrix can be written as (49)

$$J_{LC} = \begin{pmatrix} \exp\left[\frac{-2\pi i}{\lambda} n_o d\right] & 0 \\ 0 & \exp\left[\frac{-2\pi i}{\lambda} \int_0^d dz n_{Eff}\right] \end{pmatrix} \quad (13)$$

We can then combine these equations to find the total output Jones vector by(49),

$$V_{Out} = R(\varphi_1)J_P R(-\varphi_1)J_{LC}R(\varphi_2)J_P R(-\varphi_2)V_{In} \quad (14)$$

Where φ_1 and φ_2 are $\pm 45^\circ$ with respect to the rubbing direction, shown as in Fig. 1. The \pm accounts for the geometry with two crossed polarizers. The transmittance is the modulus squared of the output Jones vector. It is noteworthy that we have checked that we get the same results from the Jones Matrix Method and the transmittance equation from Scharf.

We extend the calculation to the filter by multiplying the output Jones vector by the appropriate number of additional LC Jones matrices and rotated polarizers. For our filter of two liquid crystals and three crossed polarizers, we have added one more Jones matrix for the LC and an additional rotated polarizer.

Parameters used in the calculations:

We use the Frank elastic constants $K_{11} = 12.4$ pN and $K_{33} = 24.7$ pN(53). We have experimentally measured a pre-tilt angle to be 0.04 rad. We determine an anchoring strength of $W = 2 \times 10^{-4}$ J/m² best matches the experiment. For the Cauchy coefficients, we use $A_e = 1.6950$, $B_e = -0.0015 \mu\text{m}^2$, $C_e = 0.0035 \mu\text{m}^4$, $A_o = 1.5200$, $B_o = -0.0212 \mu\text{m}^2$ and $C_o = 0.0044 \mu\text{m}^4$ which were obtained for MLC-2048 (54). Dielectric parameters used in calculations as a function of biasing field frequency presented in Table 3.

Table 3. Dielectric values of MLC-2048 as a function of the frequency of applied field (55).

Frequency of applied field (kHz)	ϵ_{\parallel}	ϵ_{\perp}	$\Delta\epsilon$
1	11.1	8.07	3.03
3	10.1	8.04	2.06
5	10.14	8.04	2.1

9	9.72	8.02	1.7
---	------	------	-----

ACKNOWLEDGMENTS: The authors thank Dr. D. Bueno-Baques and Dr. J. Nobles for help with electronic components used for the biasing box, and Rosa Machado and Justin Bendesky for the help with TIRF microscopy. Research reported in this publication was supported by the National Institute of General Medical Science of the National Institutes of Health under award number 1R15GM128166-01.

References

- (1) Booth, M. J. Adaptive Optical Microscopy: The Ongoing Quest for a Perfect Image. *Light: Sci. Appl.* **2014**, 3 (January), 1–7. <https://doi.org/10.1038/lisa.2014.46>.
- (2) Gat, N. Imaging Spectroscopy Using Tunable Filters: A Review. In *Proceedings of SPIE Wavelet Applications VII*; 2000; Vol. 4056, pp 50–64. <https://doi.org/10.1117/12.381686>.
- (3) Balas, C. Review of Biomedical Optical Imaging - A Powerful, Non-Invasive, Non-Ionizing Technology for Improving in Vivo Diagnosis. *Meas. Sci. Technol.* **2009**, 20 (10), 104020 (1-12). <https://doi.org/10.1088/0957-0233/20/10/104020>.
- (4) Yang, G.; Billmers, R. I.; Herczfeld, P. R.; Contarino, V. M. Temporal Characteristics of Narrow-Band Optical Filters and Their Application in Lidar Systems. *Opt. Lett.* **1997**, 22 (6), 414–416. <https://doi.org/10.1364/ol.22.000414>.
- (5) Hoffman, D. S.; Repasky, K. S.; Reagan, J. A.; Carlsten, J. L. Development of a High Spectral Resolution Lidar Based on Confocal Fabry-Perot Spectral Filters. *Appl. Opt.* **2012**, 51 (25), 6233–6244. <https://doi.org/10.1364/AO.51.006233>.
- (6) Kobrinski, H.; Cheung, K. W. Wavelength-Tunable Optical Filters: Applications and Technologies. *IEEE Commun. Mag.* **1989**, 27 (10), 53–63. <https://doi.org/10.1109/35.35922>.
- (7) Ovvyan, A. P.; Gruhler, N.; Ferrari, S.; Pernice, W. H. P. Cascaded Mach–Zehnder Interferometer Tunable Filters. *J. Opt.* **2016**, 18 (6), 064011(1-7). <https://doi.org/10.1088/2040-8978/18/6/064011>.
- (8) Harris, S. E.; Wallace, R. W. Acousto-Optic Tunable Filter. *J. Opt. Soc. Am.* **1969**, 59 (6), 744–747. <https://doi.org/https://doi.org/10.1364/JOSA.59.000744>.
- (9) Stratis, D. N.; Eland, K. L.; Carter, J. C.; Tomlinson, S. J.; Angel, S. M. Comparison of Acousto-

Optic and Liquid Crystal Tunable Filters for Laser-Induced Breakdown Spectroscopy. *Appl. Spectrosc.* **2001**, 55 (8), 999–1004. <https://doi.org/10.1366/0003702011953144>.

- (10) Sahli, S.; Hayward, J.; Fang, Q.; Abdlaty, R. M. Y. M. Hyperspectral Imaging: Comparison of Acousto-Optic and Liquid Crystal Tunable Filters. In *Medical Imaging 2018: Physics of Medical Imaging*; Chen, G.-H., Lo, J. Y., Gilat Schmidt, T., Eds.; SPIE, 2018; Vol. 10573, pp 10573P(1-9). <https://doi.org/10.1117/12.2282532>.
- (11) Morris, H. R.; Hoyt, C. C.; Treado, P. J. Imaging Spectrometers for Fluorescence and Raman Microscopy: Acousto-Optic and Liquid Crystal Tunable Filters. *Appl. Spectrosc.* **1994**, 48 (7), 857–866.
- (12) Wu, S.-T. Design of a Liquid Crystal Based Tunable Electrooptic Filter. *Appl. Opt.* **1989**, 28 (1), 48–52. <https://doi.org/10.1364/ao.28.000048>.
- (13) Xia, X.; Stockley, J. E.; Ewing, T. K.; Serati, S. A. Advances in Polarization-Based Liquid Crystal Optical Filters. In *Liquid Crystal Materials, Devices, and Applications VIII*; Chien, L.-C., Ed.; SPIE, 2002; Vol. 4658, pp 51–58. <https://doi.org/10.1117/12.467444>.
- (14) Shabtay, G.; Eidinger, E.; Zalevsky, Z.; Mendlovic, D.; Marom, E. Tunable Birefringent Filters - Optimal Iterative Design. *Opt. Express* **2002**, 10 (26), 1534–1541. <https://doi.org/10.1364/oe.10.001534>.
- (15) Ho, I.; Pan, C.; Hsieh, C.; Pan, R. Liquid-Crystal-Based Terahertz Tunable Solc Filter. *Opt. Lett.* **2008**, 33 (13), 1401–1403.
- (16) Jullien, A.; Pascal, R.; Bortolozzo, U.; Forget, N.; Residori, S. High-Resolution Hyperspectral Imaging with Cascaded Liquid Crystal Cells. *Optica* **2017**, 4 (4), 400–405. <https://doi.org/10.1364/optica.4.000400>.
- (17) Abuleil, M.; Abdulhalim, I. Narrowband Multispectral Liquid Crystal Tunable Filter. *Opt. Lett.*

2016, 41 (9), 1957. <https://doi.org/10.1364/ol.41.001957>.

- (18) Stoltzfus, C.; Barbour, R.; Atherton, D.; Barber, Z. Micro-Sized Tunable Liquid Crystal Optical Filters. *Opt. Lett.* **2017**, 42 (11), 2090–2093. <https://doi.org/10.1364/ol.42.002090>.
- (19) Zhang, H.; Muhammad, A.; Luo, J.; Tong, Q.; Lei, Y.; Zhang, X.; Sang, H.; Xie, C. Electrically Tunable Infrared Filter Based on the Liquid Crystal Fabry–Perot Structure for Spectral Imaging Detection. *Appl. Opt.* **2014**, 53 (25), 5632. <https://doi.org/10.1364/ao.53.005632>.
- (20) Aharon, O.; Safrani, A.; Moses, R.; Abdulhalim, I. Liquid Crystal Tunable Filters and Polarization Controllers for Biomedical Optical Imaging. *Liq. Cryst. XII* **2008**, 7050 (August 2008), 70500P. <https://doi.org/10.1117/12.795388>.
- (21) Shriyan, S. K.; Schundler, E.; Schwarze, C.; Fontecchio, A. K. Electro-Optic Polymer Liquid Crystal Thin Films for Hyperspectral Imaging. *J. Appl. Remote Sens.* **2012**, 6 (1), 063549(1-10). <https://doi.org/10.1117/1.jrs.6.063549>.
- (22) Huang, Y.; Sun, Q.; Zhang, S. Widely Tunable Optical Filter with Variable Bandwidth Based on Spatially Distributed Cholesteric Liquid Crystal. *Opt. Eng.* **2013**, 52 (4), 044003. <https://doi.org/10.1117/1.OE.52.4.044003>.
- (23) Dik, V. P.; Loïko, V. A. Spectral Characteristics of Tunable IR Liquid-Crystal Filters Based on the Christiansen Effect. *J. Opt. Technol.* **2015**, 82 (9), 602–606. <https://doi.org/10.1364/jot.82.000602>.
- (24) Nasehi, Z.; Nozhat, N. Liquid Crystal Based Tunable Plasmonic Subtractive Color Filters. *Opt. Commun.* **2019**, 445 (March), 96–100. <https://doi.org/10.1016/j.optcom.2019.04.012>.
- (25) Melnyk, O.; Garbovskiy, Y.; Bueno-Baques, D.; Glushchenko, A. Electro-Optical Switching of Dual-Frequency Nematic Liquid Crystals: Regimes of Thin and Thick Cells. *Crystals* **2019**, 9 (6), 314–322.

- (26) Xianyu, H.; Wu, S. T.; Lin, C. L. Dual Frequency Liquid Crystals: A Review. *Liq. Cryst.* **2009**, *36* (6–7), 717–726. <https://doi.org/10.1080/02678290902755598>.
- (27) Duan, W.; Chen, P.; Wei, B.-Y.; Ge, S.-J.; Liang, X.; Hu, W.; Lu, Y.-Q. Fast-Response and High-Efficiency Optical Switch Based on Dual-Frequency Liquid Crystal Polarization Grating. *Opt. Mater. Express* **2016**, *6* (2), 597. <https://doi.org/10.1364/ome.6.000597>.
- (28) Kumar, P.; Kang, S.-W.; Lee, S. H. Advanced Bistable Cholesteric Light Shutter with Dual Frequency Nematic Liquid Crystal. *Opt. Mater. Express* **2012**, *2* (8), 1121. <https://doi.org/10.1364/ome.2.001121>.
- (29) Morris, H. R.; Hoyt, C. C.; Treado, P. J. Imaging Spectrometers for Fluorescence and Raman Microscopy: Acousto-Optic and Liquid Crystal Tunable Filters. *Appl. Spectrosc.* **1994**, *48* (7), 857–866. <https://doi.org/10.1366/0003702944029820>.
- (30) Dandin, M.; Abshire, P.; Smela, E. Optical Filtering Technologies for Integrated Fluorescence Sensors. *Lab Chip* **2007**, *7* (8), 955–977. <https://doi.org/10.1039/b704008c>.
- (31) Hou, S.; Johnson, C.; Welsher, K. Real-Time 3D Single Particle Tracking: Towards Active Feedback Single Molecule Spectroscopy in Live Cells. *Molecules*. MDPI AG August 2, 2019, pp 2826(1-25). <https://doi.org/10.3390/molecules24152826>.
- (32) Ohara-Imaizumi, M.; Nishiwaki, C.; Kikuta, T.; Kumakura, K.; Nakamichi, Y.; Nagamatsu, S. Site of Docking and Fusion of Insulin Secretory Granules in Live MIN6 β Cells Analyzed by TAT-Conjugated Anti-Syntaxin 1 Antibody and Total Internal Reflection Fluorescence Microscopy. *J. Biol. Chem.* **2004**, *279* (9), 8403–8408. <https://doi.org/10.1074/jbc.M308954200>.
- (33) Renz, M. Fluorescence Microscopy-A Historical and Technical Perspective. *Cytometry. Part A* **2013**, *83* (9), 767–779. <https://doi.org/10.1002/cyto.a.22295>.
- (34) Lyot, B. Le Filtre Monochromatique Polarisant et Ses Applications En Physique Solaire. *Ann.*

D'Astrophysiqye **1944**, 667 (1–2), 31–74.

- (35) Solc, I. Birefringent Chain Filters. *J. Opt. Soc. Am.* **1965**, 55 (6), 621–625.
<https://doi.org/10.1097/00007611-192203000-00016>.
- (36) *Liquid Crystals: Experimental Study of Physical Properties and Phase Transitions*; Kumar, S., Ed.; Cambridge University Press: Cambridge, 2000.
- (37) Abdulhalim, I. Non-Display Bio-Optic Applications of Liquid Crystals. *Liq. Cryst. Today* **2011**, 20 (2), 44–60. <https://doi.org/10.1080/1358314X.2011.563975>.
- (38) Blinov, L. M. Electro-Optical Effects in Liquid Crystals. *Sov. Phys. Uspekhi* **1975**, 17 (5), 658–672.
- (39) Blinov, L. M.; Chigrinov, V. G. *Electrooptic Effects in Liquid Crystal Materials*; Springer: New-York, 1993. <https://doi.org/10.1007/978-1-4612-2692-5>.
- (40) Wu, S. T.; Wu, C. S. High-Speed Liquid-Crystal Modulators Using Transient Nematic Effect. *J. Appl. Phys.* **1989**, 65 (2), 527–532. <https://doi.org/10.1063/1.343135>.
- (41) Machado, R.; Bendesky, J.; Brown, M.; Spendier, K.; Hagen, G. M. Imaging Membrane Curvature inside a FcεRI-Centric Synapse in RBL-2H3 Cells Using TIRF Microscopy with Polarized Excitation. *J. Imaging* **2019**, 5 (7), 63(1-12). <https://doi.org/10.3390/jimaging5070063>.
- (42) Demmerle, J.; Wegel, E.; Schermelleh, L.; Dobbie, I. M. Assessing Resolution in Super-Resolution Imaging. *Methods* **2015**, 88, 3–10. <https://doi.org/10.1016/j.ymeth.2015.07.001>.
- (43) Bruyneel, F.; De Smet, H.; Vanfleteren, J.; Van Calster, A. Method for Measuring the Cell Gap in Liquid-Crystal Displays. *Opt. Eng.* **2001**, 40 (2), 259–267. <https://doi.org/10.1117/1.1337036>.
- (44) Rapini, A.; Papoular, M. Distortion D' Une Laelle Nematique Sous Champ Magnetique Conditions D' Ancrage Aux Parois. *J. Phys.* **1969**, 30 (C4), 54–56.

- (45) Yang, D.-K.; Wu, S.-T. *Fundamentals of Liquid Crystal Devices*, Second Edi.; Wiley, 2015.
- (46) Oseen, C. W. The Theory of Liquid Crystals. *Trans. Faraday Soc.* **1933**, *29*, 883–899.
- (47) Frank, F. C. On the Theory of Liquid Crystals. *Discuss. Faraday Soc.* **1958**, *25*, 19–28.
- (48) Scolari, L.; Bjarklev, A. O.; Eskildsen, L.; Alkeskjold, T. T. *Liquid Crystals in Photonic Crystal Fibers: Fabrication, Characterization and Devices*, Technical University of Denmark, 2009.
- (49) Scharf, T. *Polarized Light in Liquid Crystals and Polymers*; Wiley, 2007.
- (50) Li, J.; Wu, S. Extended Cauchy Equations for the Refractive Indices of Liquid Crystals. *J. Appl. Phys.* **2004**, *95* (3), 896–901.
- (51) Stickler, B. A.; Schachinger, E. *Basic Concepts in Computational Physics*, Second Edi.; Springer, 2016.
- (52) Boole, G. *A Treatise On the Calculus of Finite Differences*; Cambridge: London, 1860.
- (53) Wang, C.-T.; Tam, A.; Tseng, M.-C.; Lee, C.-Y.; Lin, T.-H.; Kwork, H.-S. Bistable Switching of Polarization-Grating Diffractions Enabled by a Front Bistable Twisted Nematic Film. *Opt. Lett.* **2019**, *44* (2), 187–190. <https://doi.org/https://doi.org/10.1364/OL.44.000187>.
- (54) Xiong, J.; Chen, R.; Wu, S.-T. Device Simulation of Liquid Crystal Polarization Gratings. *Opt. Express* **2019**, *27* (13), 18102–18112. <https://doi.org/https://doi.org/10.1364/OE.27.018102>.
- (55) Yin, Y.; Shiyanovskii, S. V.; Golovin, A. B.; Lavrentovich, O. D. Dielectric Torque and Orientation Dynamics of Liquid Crystals with Dielectric Dispersion. *Phys. Rev. Lett.* **2005**, *95* (8), 087801(1-4). <https://doi.org/10.1103/PhysRevLett.95.087801>.

Table of Content graphic

